Chemical Science

ROYAL SOCIETY OF CHEMISTRY

EDGE ARTICLE

View Article Online
View Journal

Cite this: DOI: 10.1039/d5sc06899a

All publication charges for this article have been paid for by the Royal Society of Chemistry

Received 7th September 2025
Accepted 25th November 2025

DOI: 10.1039/d5sc06899a

rsc.li/chemical-science

Dual activation of CO_2 and N_2 facilitated by single Ta_4^+ clusters

Yifan Gao, [ab] Ran Cheng, [ab] Klavs Hansen [c] and Zhixun Luo *[ab]

Governing molecular activation and reaction selectivity is a fundamental strategy for advancing catalytic performance. Metal clusters show great promise for tailoring reactions due to their unique electronic structures, yet the microscopic mechanisms of how their active sites cooperate are still not fully elucidated. This work examines the reactivity of Ta_n^+ clusters with CO_2 and N_2, demonstrating the dual activation of CO_2 and N_2 by individual Ta_4^+ clusters, resulting in N–O coupling. Through electron localisation function (ELF) and multi-centre bonding analyses, we elucidate how delocalised electrons and charge distribution of such metal clusters govern the reaction selectivity and stabilise intermediates along the reaction pathways. This work enhances our comprehension of cluster catalysis and offers a framework to design efficient catalysts for dual activation of CO_2 and N_2.

Introduction

In light of the challenges posed by global climate change and the continued energy requirement, the reduction of carbon dioxide (CO_2)[1–5] and nitrogen (N_2),[6–12] as pivotal subjects within green chemistry, necessitates the urgent advancement of efficient and sustainable catalytic technologies. Conventional catalytic methods, exemplified by the Haber–Bosch process,[13] while prevalent in industry, face limitations in long-term viability due to their substantial energy consumption and environmental pollution concerns. Up to now, the experimental pursuit of highly efficient and low-energy catalytic systems has emerged as a hot topic of research.[14–19] Meanwhile, the general mechanisms have been well established for N_2 reduction (*e.g.*, direct dissociative mechanism *vs.* associative distal/alternating pathway)[20] and CO_2 reduction (*e.g.*, direct CO_2 adsorption and activation *vs.* proton-coupled electron transfer, PCET).[21,22] Also, insights into the metal identity in diverse catalysts, electronic and geometric structures, metal–support interactions,[23,24] key intermediates, reaction path selectivity, *etc.* have been extensively studied.

Recent investigations indicate increasing interest in the dual activation of CO_2 and N_2.[25–30] However, ambiguities persist concerning the active locations and catalytic processes. Remarkable research on innovative nanocatalysts and single-atom catalysts has shown the formation of C–N or N–O coupling products during the concurrent activation of CO_2 and N_2, contingent upon the properties of the catalyst's active sites and the evolving structures during the reaction.[31,32] While the importance of N–C coupling is well known, the potential for direct N–O coupling interactions between CO_2 and N_2 may provoke new understanding of the fundamental mechanisms underlying NO_x production in atmospheric haze.[33] To comprehensively elucidate the catalytic mechanisms and establish a basis for the rational design of high-performance catalysts for dual activation of CO_2 and N_2, transition metal clusters are anticipated to function as optimal model systems.[34,35] Catalysts made of atomically precise clusters feature well-defined structures, tuneable compositions, specific coordination environments, and adjustable multi-site synergy, enabling a direct link between the electronic properties of individual atoms and nanoparticles.[36–40] This shows promise for achieving precise control and high performance in both CO_2 reduction and N_2 activation.[41–50]

This study investigates the reaction dynamics of tantalum (Ta) clusters with CO_2 and N_2. Joint experimental and theoretical analyses demonstrate that both localised and delocalised electrons (*e.g.*, 3c–2e multicentre bonds) in the Ta clusters are associated with the activation of CO_2 and N_2, dictating variable C=O and N≡N dissociation pathways. CO_2 selectively adsorbs at electron-rich Ta–Ta sites, undergoing C=O cleavage *via* twisted deformation; N_2 dissociates with low energy barriers on the resulting $Ta_4O_{1,2}^+$ intermediates. Despite weaker passivation than the nitride $Ta_4N_2^+$, the intermediates of cluster oxide $Ta_4O_{1,2}^+$ preserve active sites for N–O coupling to form stable $Ta_4N_2O_2^+$. By revealing the structure–activity relationships between electronic structures and reaction pathways, our findings lay the groundwork for optimising energy-efficient and selective CO_2 and N_2 conversions. This study clarifies how charge distribution and electron localisation or delocalisation

[a]State Key Laboratory for Structural Chemistry of Unstable and Stable Species, Institute of Chemistry, Chinese Academy of Sciences, Beijing 100190, China. E-mail: zxluo@iccas.ac.cn

[b]University of Chinese Academy of Sciences, Beijing 100049, China

[c]Centre for Joint Quantum Studies, Department of Physics, School of Science, Tianjin University, 92 Weijin Road, Tianjin 300072, China

control reaction selectivity and intermediate stability, thereby enabling more sustainable chemical processes.

Results and discussion

Fig. 1a depicts the mass spectrum of nascent Ta_n^+ clusters (n = 3–11), produced by a magnetron sputtering (MagS) cluster source in tandem with a multi-ion laminar flow tube reactor and a triple quadrupole mass spectrometer (MIFT-TQMS).[51] Fig. 1b illustrates the recorded mass spectrum resulting from the CO_2 reaction, showing a series of products including Ta_nO^+, $Ta_nO_2^+$, $Ta_nO_3^+$, and $Ta_nO_4^+$. The observation of these products indicates that the Ta_n^+ clusters readily react with CO_2 and are favourably transformed into metal oxides, along with CO removal. Fig. 1c illustrates the subsequent reactions by further introducing N_2 into the flow tube reactor. The $Ta_nO_{0-4}^+$ clusters then reacted with N_2 to yield a series of $Ta_nN_xO_y^+$ products. The inset shows the products from a typical Ta_4^+ cluster, such as Ta_4NO^+, $Ta_4N_2O^+$, and $Ta_4N_2O_2^+$. The observation of these $Ta_nN_xO_y^+$ products suggests dual activation of N_2 and CO_2, likely involving N–O coupling processes. Notably, this experiment did not exhibit a significant etching effect, likely due to the efficient cooling of the reaction products caused by the presence of enough He gas in the laminar flow tube.

The reactions of Ta_n^+ with CO_2 and N_2 to form $Ta_nN_xO_y^+$ products were also validated using ^{15}N isotope-labelled nitrogen gas (Fig. 2) and ^{18}O-labelled carbon dioxide (Fig. S1, SI). When the Ta_n^+ clusters react with a mixed reactant containing isotope-labelled $^{15}N_2$ and normal CO_2, they form $Ta_nN_xO_y^+$ products similar to those generated by adding CO_2 and N_2 sequentially. Upon the introduction of a minor flow of the $^{15}N_2/CO_2$ mixed gas, a range of nitrogen oxide products, such as Ta_nNO^+, $Ta_nN_2O^+$, and $Ta_nN_2O_2^+$, emerge in the mass spectra. When introducing a larger dose of the reactant gas, bigger clusters were etched and depleted, resulting in the persistence of the relatively stable Ta_4^+ cluster. Concurrently, the relative intensity of nitrogen oxide species associated with the clusters rose, and the diversity of nitrogen- and oxygen-containing products likewise increased. The degree of reactivity tends to decrease as the cluster size grows. This is because larger clusters have greater heat capacity and more flexible structures to dissipate energy, whereas smaller clusters have limited energy dispersal and reduced collision cooling, thus leading to shorter lifetimes of intermediates. Meanwhile, thermal dissociation threshold values are usually small for the larger clusters, allowing for incidental fragmentation.[52,53] Apart from the fruitful products of the Ta_4^+ cluster under different conditions (Fig. S2–S7, SI), distinct nitride and nitrogen oxide products of relatively weaker mass abundances were also detected on the other Ta_n^+ clusters. These Ta_n^+ clusters exhibited notably elevated reaction rates (larger than 10^{-9} cm^3 s^{-1} per molecule) with the mixed reactant of $^{15}N_2/CO_2$ under ambient conditions (Fig. S8, SI).

Notably, N_2 readily dissociates in reacting with the bare Ta_n^+ clusters (Fig. S2, SI), demonstrating high activity of such clusters for N_2 activation. This observation aligns well with previous theoretical and experimental studies, which have reported similar reactivity for small Ta clusters.[54–57] Also, the production of $Ta_nN_xO_y^+$ products is reproduced with different N_2/CO_2 ratios or different size distributions of the nascent Ta_n^+ clusters (Fig. S3, SI). Our results demonstrate that the end-on coordinated N_2 bends toward a neighbouring Ta atom. This forms an intermediate where N_2 bridges two Ta atoms along a tetrahedral Ta_4 edge, followed by N–N bond dissociation to yield two μ_3-N moieties on the neighbouring Ta_3 facets. A comparison of thermodynamic data reveals that the energy released during the adsorption of CO_2 on the Ta_4^+ cluster ($\Delta H = -0.31$ eV) and the subsequent CO removal to form Ta_4O^+ ($\Delta H = -2.23$ eV) are typically smaller than that for N_2 adsorption ($\Delta H = -0.78$ eV) and the formation of N–N dissociative $Ta_4N_2^+$ ($\Delta H = -4.77$ eV).

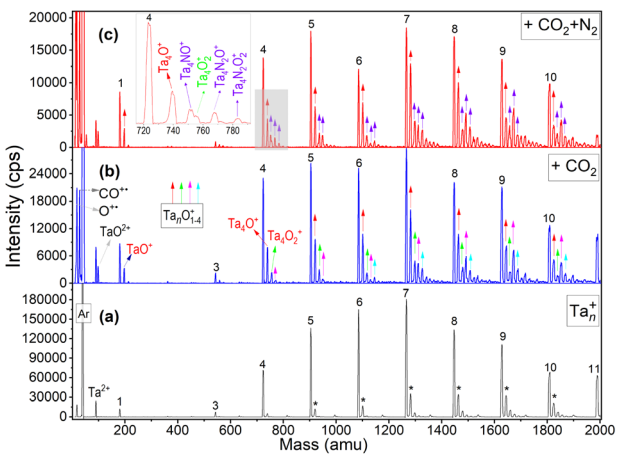

Fig. 1 (a) Mass spectrum of the nascent Ta_n^+ clusters. The stars above the mass peaks indicate oxygen contamination. (b) Mass spectra of the Ta_n^+ clusters after reactions with CO_2 (1% in He) and (c) then N_2 (1% in He) in the same flow tube reactor (~0.5 Torr), with a controllable flow rate of ~2 sccm for each.

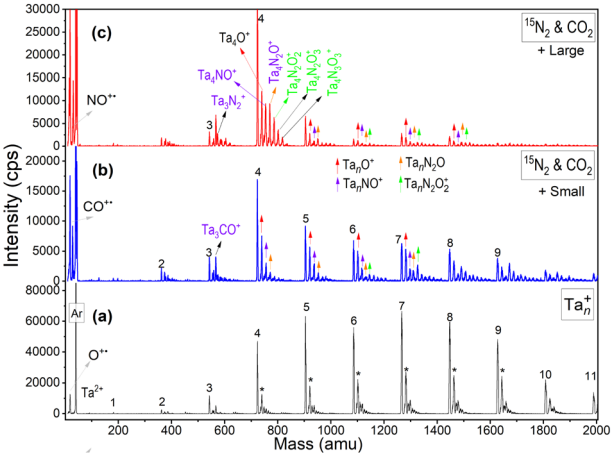

Fig. 2 (a–c) Mass spectra of the Ta_n^+ cluster before and after the reactions with a mixed reactant of N_2 and CO_2 (both 1% in He) at different flow rates (*ca.* 2 sccm and 5 sccm), introduced from the inlet of the MagS source to leverage plasma assistance. An isotopically pure reagent of $^{15}N_2$ was used to provide unambiguous mass assignments. The stars on the peaks indicate oxygen contamination.

Table 1 The energy differences of Ta_4^+ in reacting with CO_2 and N_2, calculated quantum chemically at the tpsstpss/def2tzvp level of theory

$Ta_4^+ + CO_2 \rightarrow Ta_4CO_2^+$, $\Delta H = -0.31$ eV	$Ta_4^+ + N_2 \rightarrow Ta_4{\cdot}N_2^+$, $\Delta H = -0.78$ eV
$Ta_4^+ + CO_2 \rightarrow Ta_4O^+ + CO$, $\Delta H = -2.23$ eV	$Ta_4^+ + N_2 \rightarrow Ta_4N_2^+$, $\Delta H = -4.77$ eV
$Ta_4O^+ + CO_2 \rightarrow Ta_4O{\cdot}CO_2^+$, $\Delta H = -0.35$ eV	$Ta_4N_2^+ + CO_2 \rightarrow Ta_4N_2^+{\cdot}CO_2$, $\Delta H = -2.16$ eV
$Ta_4O^+ + CO_2 \rightarrow Ta_4O_2^+ + CO$, $\Delta H = -1.97$ eV	$Ta_4N_2^+ + CO_2 \rightarrow Ta_4N_2O^+ + CO$, $\Delta H = -1.34$ eV
$Ta_4O^+ + N_2 \rightarrow Ta_4O{\cdot}N_2^+$, $\Delta H = -1.38$ eV	$Ta_4O_2^+ + N_2 \rightarrow Ta_4O_2{\cdot}N_2^+$, $\Delta H = -0.87$ eV
$Ta_4O^+ + N_2 \rightarrow Ta_4ON_2^+$, $\Delta H = -4.23$ eV	$Ta_4O_2^+ + N_2 \rightarrow Ta_4O_2N_2^+$, $\Delta H = -4.35$ eV

However, enhanced stability of the N-capped $Ta_4N_2^+$ diminishes the likelihood of subsequent activation of CO_2 molecules ($\Delta H = -1.34$ eV), indicating that the μ_3-N exerts an effective passivation effect on the Ta_4^+ cluster. This result rebuts the traditional idea that N_2 must be added first because its stronger bond (N≡N) makes it harder to activate than CO_2 (Table 1).

In comparison, when the Ta_4^+ cluster first reacts with CO_2 to form a Ta_4O^+ intermediate ($\Delta H = -2.23$ eV), the subsequent N_2 adsorption energy is markedly exothermic ($\Delta H = -1.38$ eV). This indicates that nitrogen adheres strongly to the cluster oxide Ta_4O^+ and is less prone to desorption compared to the nascent Ta_4^+ cluster, which is beneficial for stable adsorption and subsequent N_2 activation. The N≡N dissociation energy on the Ta_4O^+ intermediate ($\Delta H = -4.23$ eV) is comparable with that on the pure Ta_4^+ cluster, establishing an energetic basis for the amalgamation of nitrogen and oxygen atoms within clusters. These energy changes promote the coupling of nitrogen and oxygen atoms, leading to the formation of N–O coupling products, of which the geometric and electronic structures are given in the SI (Fig. S9–S16).

Fig. 3 presents the energy diagrams comparing the potential reaction pathways for a Ta_4^+ cluster with N_2 and two CO_2 molecules. When Ta_4^+ initially reacts with N_2, it forms a stable N_2-dissociated $Ta_4N_2^+$ intermediate (Fig. 3A), which makes the subsequent CO_2 activation dynamically less favourable, with an energy barrier of 5.02 eV for N–O coupling (TS5). In comparison,

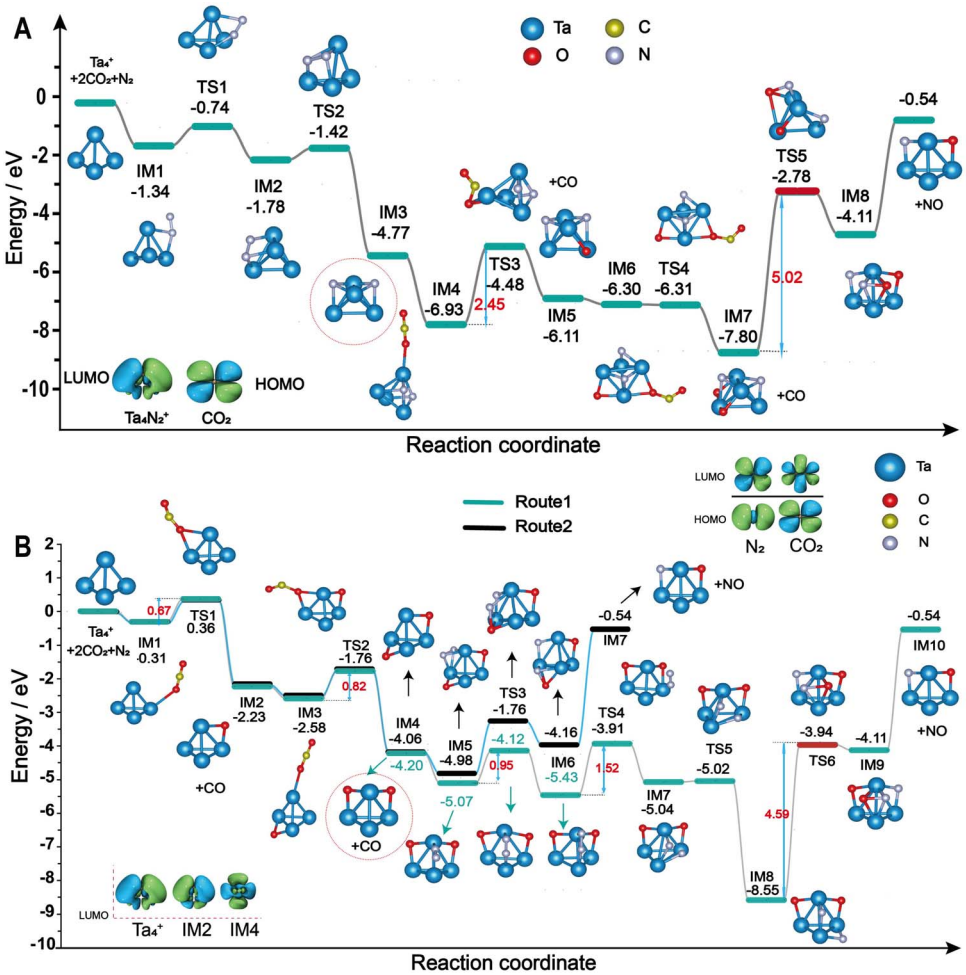

Fig. 3 (A and B) Energy reaction diagram of a Ta_4^+ cluster reacting with an N_2 and two CO_2 molecules at different sequences, ultimately yielding Ta_4NO^+ and a released NO molecule. Insets depict the LUMOs and HOMOs of the intermediates involved in the reaction process.

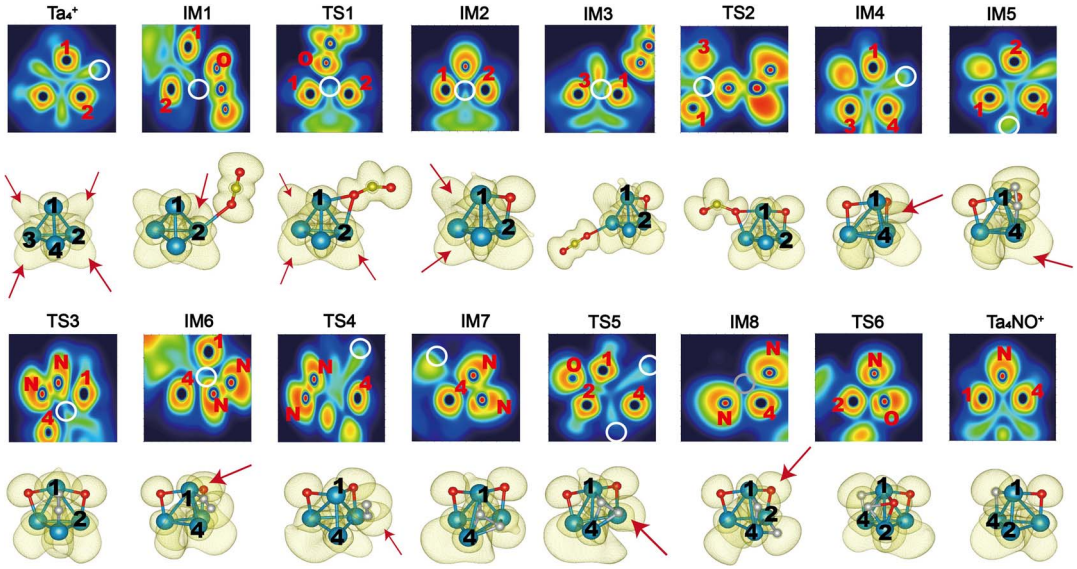

Fig. 4 The 2D and 3D electron localization functional (ELF) analyses for the intermediates (IM) and transition states (TS) during the reaction process (Route 1 in Fig. 3). In 2D-ELF, active sites are highlighted with white circles, while changes in covalent bonding are indicated by grey circles. The numerical labels on the atoms correspond to the atomic numbering within the metal cluster. In 3D-ELF, the red arrows indicate active sites, with the atoms 1, 2, 3, and 4 being kept in the same position for all.

the reaction of CO_2 first (Fig. 3B) suffers from a small single-step energy barrier for the first CO_2 dissociation (0.67 eV, TS1). Nonetheless, the formation of Ta_4O^+ along with a CO removal will result in significant energy gain (−2.23 eV, IM2). The second CO_2 adsorption and C=O bond dissociation event is more exothermic, forming a $Ta_4O_2^+$ product with two isomeric configurations (IM4). The energy gains are −4.06 eV for the *ortho*-site bridged isomer (Route 1) and −4.20 eV for the *para*-site bridged isomer (Route 2). The large energy gain for Ta_4^+ to react with two CO_2 molecules facilitates the subsequent N_2 activation. Notably, the energies for N_2 dissociation on Ta_4O^+ (Fig. S17, SI) and $Ta_4O_2^+$ (Fig. 3B) are lower than that on pure clusters. The significant decrease in energy promotes the subsequent N_2-adsorption and N≡N dissociation, and enables N–O coupling at a relatively smaller single-step energy barrier (TS6). The other reaction pathways for different sequences of CO_2 and N_2 adsorbed on the Ta_4^+ cluster all lead to similar results with a product of $Ta_4(NO)_{1,2}^+$ and the pathways for N–N dissociation and NO release ultimately are thermodynamically favourable even on a graphene support (Fig. S18–S24, SI). Additionally, the selectivity of the two reaction pathways (*i.e.*, Routes 1 and 2) was evaluated by referring to RRKM theory.[58–61] The results demonstrate a pronounced kinetic preference for Route 1, as evidenced by its significantly higher rate constant of 8.85×10^{12} s^{-1}—roughly 122 times larger than the value calculated for Route 2 (*c.a.* 7.23×10^{10} s^{-1}).

The modified electronic configurations profoundly influence the cluster's reactivity. Nitrogen's stronger electron affinity disrupts the bonding network, enhancing passivation and inhibiting further reactions. Fig. 4 presents the electron localisation function (ELF)[32,33] analysis for all the intermediate states along Route 1 (for details see Fig. S25–S34, SI), revealing the electronic coupling between small molecules and Ta_4^+ clusters throughout the whole reaction process. ELF analysis reveals uniformly distributed charges across all remaining Ta–Ta bonds at this stage. The distinctive electronic configuration of Ta_4^+ facilitates charge-driven interactions with CO_2. Initially, CO_2 interacts with Ta_4^+ to form an adsorption intermediate (IM1). Following this, the coordination of CO_2 causes distortion of the electron cloud in TS1 (μ_2-O), facilitating the cleavage of a C–O bond to form Ta_4O^+ (IM2). The incorporation of oxygen modifies the cluster's electronic configuration, resulting in greater charge localisation within the Ta–Ta bonds adjacent to the Ta–O–Ta units (specifically, Ta1–Ta3). The enhanced bonding network promotes further CO_2 adsorption, leading to the formation of the $Ta_4O_2^+$ intermediate (IM4). In addition to the considerable energy advantage of CO removal in the formation of $Ta_4O_2^+$, large charge accumulation at the metal sites of the $Ta_4O_2^+$ intermediate facilitates subsequent N_2 adsorption and activation. The increased charge density facilitates subsequent N_2 adsorption across multiple Ta–Ta sites (Fig. S36, SI). Subsequent to N_2 adsorption, charge polarisation facilitates N_2 dissociation, wherein one nitrogen atom transitions to an oxygen site *via* a transition state to yield NO. The residual nitrogen is drawn to adjacent charges, resulting in further NO production and the transformation of the cluster into Ta_4NO^+. Likewise, the reaction pathway for Route 2 was delineated using ELF analysis (Fig. S35, SI), revealing heightened charge density between neighbouring Ta–Ta bonds (Ta2–Ta3) and the connection (Ta3–Ta4). This method emphasises the synergistic effects of cluster charge redistribution and orbital overlap interactions in the catalytic dual activation of CO_2 and N_2.

This interplay between heteroatom incorporation and electronic restructuring underscores the utility of adaptive natural density partitioning (AdNDP) analysis.[62] Notably, the frontier

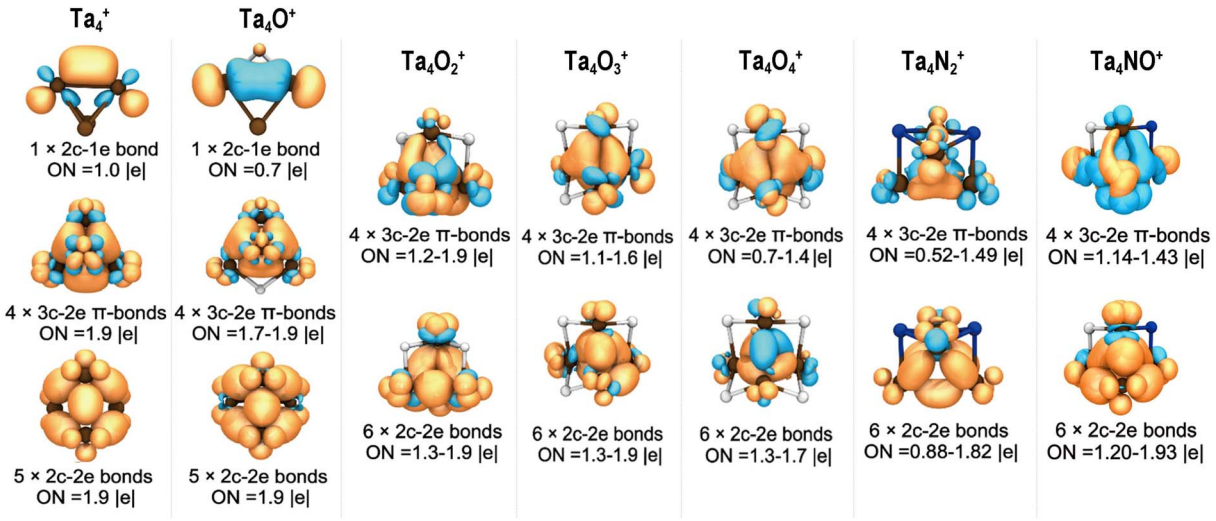

Fig. 5 AdNDP bonding analysis of the Ta_4^+, $Ta_4O_{1-4}^+$, $Ta_4N_2^+$ and Ta_4NO^+ clusters. The occupation numbers (ON) are given below each pattern.

orbitals of N_2 and CO_2 align well with those of the nascent Ta_4^+ and subsequent intermediates (IM2 and IM4), promoting the formation of coordination bonds once adsorbed. Previous studies have demonstrated the mechanisms governing such small cluster stability and structure–property relationships, including geometric structure, charge population, and surface Lewis acid/base sites, as well as electronic configuration including superatomic features, and the resulting energetics and dynamics within the surrounding environment.[57] Here, the finding of unique cluster catalysis of Ta_4^+ is largely contributed by its identical Lewis acid sites and the reduced sizes.[54–56] To fully elucidate the reaction mechanism, we analysed the bonding modes and their evolution in this small cluster reaction using AdNDP analysis, which offers a comprehensive approach to describe chemical bonding, encompassing both localised electron pairs and delocalised multi-centre bond interactions (Fig. S37–S43, SI). As illustrated in Fig. 5, the nascent Ta_4^+ cluster initially features five 2c–2e bonds and four 3c–2e bonds, along with a 2c–1e Ta–Ta bond due to the positive charge. The Ta_4O^+ and $Ta_4O_2^+$ intermediates preserve the multi-centre bonds and electronic structure of Ta_4^+; however, the addition of oxygen weakens the 2c–1e bond occupancy and decreases the occupation numbers (ON) of delocalised 3c–2e bonds, indicating electron transfer to the oxygen atoms. In contrast, the $Ta_4N_2^+$ and Ta_4NO^+ clusters exhibit a more substantial disruption of 3c–2e bonding, indicative of a more pronounced effect than in $Ta_4O_{1-4}^+$ clusters. This emphasises nitrogen's stronger ability to withdraw electrons and its more significant influence on the electronic accommodation during the reaction process.

In principle, localised electrons, due to their concentrated electron density, tend to act as key active sites or reactive centres. Electron-rich regions, such as lone pairs and π-bonds, can initiate nucleophilic reactions; conversely, electron-deficient areas, like the positive end of a polar bond, can be targeted by electron-rich reagents. The well-defined bond energy of localised σ-bonds within a cluster, like Ta_4^+, allows for homolytic cleavage and radical formation. In contrast, delocalised electrons (or multicentre bonds) may function to stabilise the overall metal cluster structure, with a more even charge distribution throughout the cluster. A balance of local bonding and delocalised electrons allows for distinctive reaction pathways by stabilising crucial intermediates,[63] thereby generating energetically favourable sites for further electrophilic or nucleophilic attacks, which is particularly beneficial when multiple reactant molecules are involved.

Experimental

Experimental details

The experiments were conducted using a homemade MIFT-TQMS instrument,[64] in tandem with a customised MagS source. The MagS source was used to produce pure tantalum clusters. These clusters were then introduced into a flow tube reactor (with a diameter of 60 mm and a length of 1 meter) using high-purity helium gas (purity > 99.999%). Inside the reactor, the clusters reacted with specific reactant gases. The flow rate of the reactant gases was controlled using a gas flowmeter (Alicat) throughout the experiment. To ensure sufficient collisional interactions of the Ta_n^+ clusters, the pressure within the MagS source was kept at approximately 2.6 Torr, while the flow tube was kept at about 0.6 Torr. This was achieved by using a laminar flow of helium buffer gas from the upstream MagS source and a downstream Roots pump with a pumping speed of 142 litres per second. After the reaction, the resulting products were transferred into a differentially pumped five-stage vacuum system, equipped with different-sized apertures and linear/conical octuple ion guides, respectively. Finally, the products were analysed using a custom quadrupole mass spectrometer.

Computational details

The initial structures of the tantalum clusters were designed by examining the experimental and theoretical studies that had been previously reported in the literature while also considering

the variations in spin multiplicity and geometric structure. The Gaussian 16 program[65] was employed to conduct the structural optimisation and energetics calculations at the TPSStpss/def2-TZVP level of theory.[66] The energies were corrected by zero-point vibrations, and all the calculated low-lying isomers and intermediates were verified to ensure that there was no imaginary frequency. All transition states (TS) were confirmed to possess one imaginary frequency and correlated with the reaction pathway, which was also validated by intrinsic reaction coordinate (IRC) computations.[67] The projected density of states (pDOS) and natural population analysis (NPA) studies were conducted utilizing the Multiwfn software.[68] The VMD (Visual Molecular Dynamics) program was employed to create the figures.[69]

Conclusions

In conclusion, we have prepared well-resolved Ta_n^+ clusters (n = 4–10) and studied their gas-phase reactions with N_2 and CO_2 using a customised flow tube reactor and mass spectrometer. Our study demonstrates a direct relationship between their atomic structure and their varying reactivity with the two inert gas molecules. Interestingly, the sequential activation of CO_2 followed by N_2 by the bare Ta_4^+ cluster is facilitated by an oxygen-induced electronic reconfiguration, resulting in N–O coupling. The incorporation of one or two oxygen atoms selectively creates new, highly reactive sites on the cluster surface, which are crucial for the subsequent N_2 cleavage and coupling reactions. Conversely, the pre-formed $Ta_4N_2^+$ cluster demonstrates reduced reactivity, which is rooted in its thermodynamically stable dual μ_3-N structure. This structural motif passivates the active sites and releases more energy upon production of $Ta_4N_2^+$ in contrast to the formation of a $Ta_4O_2^+$ equivalent with μ_2-O bridge bonds. Utilising ELF and AdNDP studies, we clarify how delocalised electrons and charge distribution within these metal clusters dictate reaction selectivity and stable intermediates across the reaction pathways. The selectivity of these Ta clusters is shaped by their electronic configuration, which is affected by their geometric structures. The essential role of multi-centre bonds in facilitating dual activation of N_2 and CO_2 presents a fundamental framework for rational design of efficient Ta-based catalysts, emphasising the balance between electronic accommodation and surface passivation.

Author contributions

The manuscript was written through the contributions of all authors.

Conflicts of interest

There are no conflicts to declare.

Data availability

The data supporting this article have been included as part of the supplementary information (SI). Supplementary information: Fig. S1–S43, experimental and computational details, including mass spectrometry observations, rate constants, geometric and electronic structures, energetics, DOSs, frontier orbitals, reaction pathways, and ELF and AdNDP analyses. See DOI: https://doi.org/10.1039/d5sc06899a.

Acknowledgements

This work was supported by the National Natural Science Foundation of China (Grant No. 92261113), the CAS Project for Young Scientists in Basic Research (Grant No. YSBR-050), the CAS Key Research Program of Frontier Sciences (QYZDBSSW-SLH024), and Beijing Natural Science Foundation (Grant No. F251006).

Notes and references

1 W. Zhou, K. Cheng, J. Kang, C. Zhou, V. Subramanian, Q. Zhang and Y. Wang, *Chem. Soc. Rev.*, 2016, **48**, 3193–3228.
2 X. Kang, Q. Zhu, X. Sun, J. Hu, J. Zhang, Z. Liu and B. Han, *Chem. Sci.*, 2016, **7**, 266–273.
3 J. Wu, Y. Huang, W. Ye and Y. Li, *Adv. Sci.*, 2017, **4**, 1700194.
4 L. G. Dodson, M. C. Thompson and J. M. Weber, *Annu. Rev. Phys. Chem.*, 2018, **69**, 231–252.
5 L. Wang, W. Chen, D. Zhang, Y. Du, R. Amal, S. Qiao, J. Wu and Z. Yin, *Chem. Soc. Rev.*, 2019, **48**, 5310–5349.
6 M. Jiang, M. Zhu, M. Wang, Y. He, X. Luo, C. Wu, L. Zhang and Z. Jin, *ACS Nano*, 2023, **17**, 3209–3224.
7 D. V. Yandulov and R. R. Schrock, *Science*, 2003, **301**, 76–78.
8 D. Bao, Q. Zhang, F.-L. Meng, H.-X. Zhong, M.-M. Shi, Y. Zhang, J.-M. Yan, Q. Jiang and X.-B. Zhang, *Adv. Mater.*, 2017, **29**, 1604799.
9 J. Deng, J. A. Iñiguez and C. Liu, *Joule*, 2018, **2**, 846–856.
10 M.-A. Legare, G. Belanger-Chabot, R. D. Dewhurst, E. Welz, I. Krummenacher, B. Engels and H. Braunschweig, *Science*, 2018, **359**, 896–899.
11 C. Liu, Q. Li, C. Wu, J. Zhang, Y. Jin, D. R. MacFarlane and C. Sun, *J. Am. Chem. Soc.*, 2019, **141**, 2884–2888.
12 G. Qing, R. Ghazfar, S. T. Jackowski, F. Habibzadeh, M. M. Ashtiani, C.-P. Chen, M. R. Smith III and T. W. Hamann, *Chem. Rev.*, 2020, **120**, 5437–5516.
13 C. M. Goodwin, P. Lömker, D. Degerman, B. Davies, M. Shipilin, F. Garcia-Martinez, S. Koroidov, J. Katja Mathiesen, R. Rameshan, G. L. S. Rodrigues, C. Schlueter, P. Amann and A. Nilsson, *Nature*, 2024, **625**, 282–286.
14 T. Wu, X. Zhu, Z. Xing, S. Mou, C. Li, Y. Qiao, Q. Liu, Y. Luo, X. Shi, Y. Zhang and X. Sun, *Angew. Chem., Int. Ed.*, 2019, **58**, 18449–18453.
15 M.-M. Shi, D. Bao, B.-R. Wulan, Y.-H. Li, Y.-F. Zhang, J.-M. Yan and Q. Jiang, *Adv. Mater.*, 2017, **29**, 1606550.
16 H. Cheng, L.-X. Ding, G.-F. Chen, L. Zhang, J. Xue and H. Wang, *Adv. Mater.*, 2018, **30**, 1803694.
17 Y. Guo, T. Wang, Q. Yang, X. Li, H. Li, Y. Wang, T. Jiao, Z. Huang, B. Dong, W. Zhang, J. Fan and C. Zhi, *ACS Nano*, 2020, **14**, 9089–9097.
18 J. Gu, C.-S. Hsu, L. Bai, H. M. Chen and X. Hu, *Science*, 2019, **364**, 1091–1094.

19 L.-H. Mou, Y. Li, G.-P. Wei, Z.-Y. Li, Q.-Y. Liu, H. Chen and S.-G. He, *Chem. Sci.*, 2022, **13**, 9366–9372.
20 C. Cui, H. Zhang, R. Cheng, B. Huang and Z. Luo, *ACS Catal.*, 2022, **12**, 14964–14975.
21 G. Liu, P. Poths, X. Zhang, Z. Zhu, M. Marshall, M. Blankenhorn, A. N. Alexandrova and K. H. Bowen, *J. Am. Chem. Soc.*, 2020, **142**, 7930–7936.
22 X.-Y. He, Y.-Z. Liu, J.-J. Chen, X. Lan, X.-N. Li and S.-G. He, *J. Phys. Chem. Lett.*, 2023, **14**, 6948–6955.
23 M. Xu, M. Peng, H. Tang, W. Zhou, B. Qiao and D. Ma, *J. Am. Chem. Soc.*, 2024, **146**, 2290–2307.
24 H. Miura, K. Imoto, H. Nishio, A. Junkaew, Y. Tsunesada, Y. Fukuta, M. Ehara and T. Shishido, *J. Am. Chem. Soc.*, 2024, **146**, 27528–27541.
25 C. Chen, X. Zhu, X. Wen, Y. Zhou, L. Zhou, H. Li, L. Tao, Q. Li, S. Du, T. Liu, D. Yan, C. Xie, Y. Zou, Y. Wang, R. Chen, J. Huo, Y. Li, J. Cheng, H. Su, X. Zhao, W. Cheng, Q. Liu, H. Lin, J. Luo, J. Chen, M. Dong, K. Cheng, C. Li and S. Wang, *Nat. Chem.*, 2020, **12**, 717–724.
26 M. Yuan, J. Chen, Y. Xu, R. Liu, T. Zhao, J. Zhang, Z. Ren, Z. Liu, C. Streb, H. He, C. Yang, S. Zhang and G. Zhang, *Energy Environ. Sci.*, 2021, **14**, 6605–6615.
27 M. Yuan, J. Chen, Y. Bai, Z. Liu, J. Zhang, T. Zhao, Q. Wang, S. Li, H. He and G. Zhang, *Angew. Chem., Int. Ed.*, 2021, **60**, 10910–10918.
28 M. Wang, L.-Y. Chu, Z.-Y. Li, A. M. Messinis, Y.-Q. Ding, L. Hu and J.-B. Ma, *J. Phys. Chem. Lett.*, 2021, **12**, 3490–3496.
29 P. Xing, S. Wei, Y. Zhang, X. Chen, L. Dai and Y. Wang, *ACS Appl. Mater. Interfaces*, 2023, **15**, 22101–22111.
30 X. Song, C. Basheer, Y. Xia, J. Li, I. Abdulazeez, A. A. Al-Saadi, M. Mofidfar, M. A. Suliman and R. N. Zare, *J. Am. Chem. Soc.*, 2023, **145**, 25910–25916.
31 Y. Yao, Z. Sun, T. Li, Z. Zhao, Z. Li, X. Lu, Y. Wan, Y. Fan and Z. Chen, *ACS Nano*, 2025, **19**, 18947–18975.
32 F. Hu, L. Yang, Y. Jiang, C. Duan, X. Wang, L. Zeng, X. Lv, D. Duan, Q. Liu, T. Kong, J. Jiang, R. Long and Y. Xiong, *Angew. Chem., Int. Ed.*, 2021, **60**, 26122–26127.
33 Q. Yi, C. Cui, D. Ma and Z. Luo, *Inorg. Chem.*, 2025, **64**, 4082–4089.
34 Z. Luo and A. Shehzad, *ChemPhysChem*, 2024, **25**, e202300715.
35 A. E. Green, J. Justen, W. Schöllkopf, A. S. Gentleman, A. Fielicke and S. R. Mackenzie, *Angew. Chem., Int. Ed.*, 2018, **57**, 14822–14826.
36 G. Frenking, I. Fernández, N. Holzmann, S. Pan, I. Krossing and M. Zhou, *JACS Au*, 2021, **1**, 623–645.
37 Y. Lu, W.-Z. Yang, X.-X. Ding, S.-Q. Nie, Z.-G. Jiang and C.-H. Zhan, *Dalton Trans.*, 2023, **52**, 13063–13067.
38 C. Cui, Y. Jia, S. Lin, L. Geng and Z. Luo, *Small*, 2024, **20**, 2404638.
39 L. Xiao, Q. Zheng, S. Luo, Y. Ying, R. Zhou, S. Zhou, X. Li, X. Ye, Z. Yu, Q. Xu, H. Liao and J. Xu, *Sci. Adv.*, 2024, **10**, eadn2707.
40 M. K. Mohanta and P. Jena, *Nanoscale*, 2025, **17**, 8505–8514.
41 B. Li, M. Chen, Q. Hu, J. Zhu, X. Yang, Z. Li, C. Hu, Y. Li, P. Ni and Y. Ding, *Appl. Catal., B*, 2024, **346**, 123733.
42 Y. Du, C. Li, Y. Dai, H. Yin and M. Zhu, *Nanoscale Horiz.*, 2024, **9**, 1262–1278.
43 W.-P. Chen, K.-P. Bai, M.-T. Lv, S. Ni, C. Huang, Q.-Y. Yang and Y.-Z. Zheng, *Angew. Chem., Int. Ed.*, 2025, **64**, e202424805.
44 H. Tao, C. Choi, L.-X. Ding, Z. Jiang, Z. Han, M. Jia, Q. Fan, Y. Gao, H. Wang, A. W. Robertson, S. Hong, Y. Jung, S. Liu and Z. Sun, *Chem*, 2019, **5**, 204–214.
45 J. K. Li, J. P. Dong, S. S. Liu, Y. Hua, X. L. Zhao, Z. Li, S. N. Zhao, S. Q. Zang and R. Wang, *Angew. Chem., Int. Ed.*, 2024, **63**, e202412144.
46 Y. F. Lu, L. Z. Dong, J. Liu, R. X. Yang, J. J. Liu, Y. Zhang, L. Zhang, Y. R. Wang, S. L. Li and Y. Q. Lan, *Angew. Chem., Int. Ed.*, 2021, **60**, 26210–26217.
47 L. Qin, F. Sun, X. Ma, G. Ma, Y. Tang, L. Wang, Q. Tang, R. Jin and Z. Tang, *Angew. Chem., Int. Ed.*, 2021, **60**, 26136–26141.
48 Y. Sun, Z. Luo and J. Qiu, *Angew. Chem., Int. Ed.*, 2024, **63**, e202406879.
49 Q. J. Wu, D. H. Si, P. P. Sun, Y. L. Dong, S. Zheng, Q. Chen, S. H. Ye, D. Sun, R. Cao and Y. B. Huang, *Angew. Chem., Int. Ed.*, 2023, **62**, e202306822.
50 S. Zhuang, D. Chen, L. Liao, Y. Zhao, N. Xia, W. Zhang, C. Wang, J. Yang and Z. Wu, *Angew. Chem., Int. Ed.*, 2020, **59**, 3073–3077.
51 H. Zhang, H. Wu, Y. Jia, L. Geng, Z. Luo, H. Fu and J. Yao, *Rev. Sci. Instrum.*, 2019, **90**, 073101.
52 B. Yoon, P. Koskinen, B. Huber, O. Kostko, B. von Issendorff, H. Hakkinen, M. Moseler and U. Landman, *ChemPhysChem*, 2007, **8**, 157–161.
53 M. Yang, H. Wu, B. Huang and Z. Luo, *J. Phys. Chem. A*, 2019, **123**, 6921–6926.
54 C. Geng, J. Li, T. Weiske and H. Schwarz, *Proc. Natl. Acad. Sci. U. S. A.*, 2018, **115**, 11680–11687.
55 D. V. Fries, M. P. Klein, A. Steiner, M. H. Prosenc and G. Niedner-Schatteburg, *Phys. Chem. Chem. Phys.*, 2021, **23**, 11345–11354.
56 D. V. Fries, M. P. Klein, A. Strassner, M. E. Huber, M. Luczak, C. Wiehn and G. Niedner-Schatteburg, *J. Chem. Phys.*, 2023, **159**, 164303.
57 R. Cheng, Y. Gao, C. Cui and Z. Luo, *J. Phys. Chem. Lett.*, 2025, **16**, 454–459.
58 R. A. Marcus, *J. Chem. Phys.*, 1952, **20**, 359–364.
59 S. K. Gray, S. A. Rice and M. J. Davis, *J. Phys. Chem.*, 1986, **90**, 3470–3482.
60 J. Westergren, H. Grönbeck, S.-G. Kim and D. Tománek, *J. Chem. Phys.*, 1997, **107**, 3071–3079.
61 B. Huang, W. Gan, K. Hansen and Z. Luo, *J. Phys. Chem. A*, 2022, **126**, 4801–4809.
62 T. Lu and F. Chen, *J. Comput. Chem.*, 2012, **33**, 580–592.
63 S. Lin, D. Li, D. Zhang, L. Geng, Y. Jia, W. Wang, L. Cheng, S. N. Khanna and Z. Luo, *Chem. Sci.*, 2025, **16**, 11619–11625.
64 B. Huang, H. Wu, M. Yang and Z. Luo, *Rev. Sci. Instrum.*, 2022, **93**, 113307.
65 M. J. Frisch, G. W. Trucks, H. B. Schlegel, G. E. Scuseria, M. A. Robb, J. R. Cheeseman, G. Scalmani, V. Barone, G. A. Petersson, H. Nakatsuji, X. Li, M. Caricato, A. V. Marenich, J. Bloino, B. G. Janesko, R. Gomperts,

B. Mennucci, H. P. Hratchian, J. V. Ortiz, A. F. Izmaylov, J. L. Sonnenberg, D. Williams-Young, F. Ding, F. Lipparini, F. Egidi, J. Goings, B. Peng, A. Petrone, T. Henderson, D. Ranasinghe, V. G. Zakrzewski, J. Gao, N. Rega, G. Zheng, W. Liang, M. Hada, M. Ehara, K. Toyota, R. Fukuda, J. Hasegawa, M. Ishida, T. Nakajima, Y. Honda, O. Kitao, H. Nakai, T. Vreven, K. Throssell, J. A. Montgomery Jr, J. E. Peralta, F. Ogliaro, M. J. Bearpark, J. J. Heyd, E. N. Brothers, K. N. Kudin, V. N. Staroverov, T. A. Keith, R. Kobayashi, J. Normand, K. Raghavachari, A. P. Rendell, J. C. Burant, S. S. Iyengar, J. Tomasi, M. Cossi, J. M. Millam, M. Klene, C. Adamo, R. Cammi, J. W. Ochterski, R. L. Martin, K. Morokuma, O. Farkas, J. B. Foresman and D. J. Fox, *Gaussian 16 Rev. B.01*, Gaussian, Inc., Wallingford, CT, 2016.

66 J. Wu, J. Hu, Q. Liu, Y. Tang, Y. Liu, W. Xiang, S. Sun and Z. Suo, *J. Mol. Model.*, 2024, **30**, 33.

67 C. Gonzalez and H. B. Schlegel, *J. Chem. Phys.*, 1989, **90**, 2154–2161.

68 T. Lu, *J. Chem. Phys.*, 2024, **161**, 082503.

69 W. Humphrey, A. Dalke and K. Schulten, *J. Mol. Graph.*, 1996, **14**, 33–38.